Determination of the yield radius and yield stress in 2198-T3 aluminum alloy by means of the dual-scale instrumented indentation test

fluids

MDPI

Article

Characterization of the Three-Dimensional Flowfield over a Truncated Linear Aerospike

Roberto Marsilio, Gaetano Maria Di Cicca, Emanuele Resta * and Michele Ferlauto

Department of Mechanical and Aerospace Engineering, Politecnico di Torino, Corso Duca degli Abruzzi 24, 10129 Torino, Italy; roberto.marsilio@polito.it (R.M.); gaetano.dicicca@polito.it (G.M.D.C.); michele.ferlauto@polito.it (M.F.)

* Correspondence: emanuele.resta@polito.it

Abstract: The work focuses on the characterization of the flowfield over a truncated linear aerospike by combining theoretical grounds, numerical simulations and experimental tests. The experimental investigations are carried out on a test rig designed at Politecnico di Torino for advanced nozzle testing. Fully three-dimensional CFD analyses are performed on the actual geometry of the experimental nozzle model. At low nozzle pressure ratios (NPRs) the analysis combines numerical simulations and experimental testing, which are also used for validating the CFD results. At higher NPRs, the flowfield characterization is performed only by three-dimensional CFD analyses. In addition to the validation of the numerical method, the edge effects at different NPRs have been observed.

Keywords: aerospike; supersonic nozzles; experimental testing; rocket nozzles

Citation: Marsilio, R.; Di Cicca, G.M.; Resta, E.; Ferlauto, M. Characterization of the Three-Dimensional Flowfield over a Truncated Linear Aerospike. *Fluids* **2024**, *9*, 179. https://doi.org/10.3390/fluids9080179

Academic Editor: Mahmoud Mamou

Received: 29 June 2024
Revised: 29 July 2024
Accepted: 8 August 2024
Published: 10 August 2024

1. Introduction

The renewed commercial and strategic interest in space has led several nations to consider the development of Reusable Propulsion Systems (RPSs) to reduce launch and production costs. In recent years, reducing the cost per kilogram of payload put into orbit has become increasingly important. Naturally, cost reduction requires the design of more sophisticated and complex launch systems compared to traditional ones. Reusable propulsion systems drive designers toward more advanced and complex design solutions, which can enhance engine performance and durability. Additionally, modern launch vehicle engines must meet the requirements for advanced control systems. These systems are essential for improving the vehicle's maneuverability, especially at low speeds, thereby enabling soft landings and the recovery of launchers [1].

In this scenario, Single-Stage-to-Orbit (SSTO) and Two-Stage-to-Orbit (TSTO) configurations are being explored as potential architectures for future launch vehicles. The feasibility of these vehicles heavily depends on the performance of their engines. Existing rocket engines frequently fail to meet theoretical performance expectations due to multiple loss mechanisms within the combustion chamber and nozzle. These include imperfect oxidizer and fuel mixing, irreversible processes within the combustion chamber, flow divergence, non-uniformity at the nozzle exit, and suboptimal propellant expansion within the nozzle. Among these factors, non-ideal expansion emerges as the most prominent contributor to performance discrepancies. For example, the Space Shuttle Main Engine (SSME) may experience a performance decrease up to 15% during critical mission phases due to the non-adaptation of exhaust gases [2].

The SSME utilizes conventional bell nozzles engineered to function seamlessly from sea-level conditions during liftoff to near-vacuum conditions in space. The Nozzle Pressure Ratio at design conditions ($\mathrm{NPR}_d = (p_c^\circ / p_a)_d$) represents a delicate balance, aiming to enhance performance at high altitudes while mitigating risks associated with uncontrolled separations and side loads during liftoff. In such scenarios, shock waves may develop

within the nozzle's divergent section, exposing the walls to substantial pressure gradients and vibrational loads, thereby posing a potential threat of launcher destruction.

The compromise in the NPR_d becomes even more restrictive for SSTO vehicles, prompting the investigation of advanced nozzle concepts as alternatives to bell nozzles. Among these alternatives, plug and aerospike nozzles stand out, offering continuous altitude adaptation up to their geometrical area ratio. For high-area ratio nozzles with relatively short lengths, plug nozzles outperform conventional bell nozzles.

Since the 1950s, extensive experimental, analytical, and numerical research has been conducted on plug nozzles worldwide [3–8].

A notable historical example is the linear aerospike engine XRS-2200, which was considered for the Venture Star/X-33 SSTO spaceplane in the 1990s. However, research on aerospike engines dwindled following the cancellation of several programs. Recently, the CALVEIN (California Launch Vehicle Education Initiative) project analyzed a truncated plug nozzle in a comprehensive test campaign [9]. Additionally, various designs for aerospike engines have been proposed for SSTO and TSTO vehicles, including those from Firefly Aerospace, RocketStar Space, and ARCA Space Corporation. Aerospike nozzles are particularly associated with propulsion for high-speed aircraft and trans-atmospheric flight due to their vectored thrust capabilities [10]. An aerospike nozzle can feature a toroidal chamber and throat, with or without truncation, and it may be equipped with a cluster of circular bell nozzle modules or clustered quasi-rectangular nozzle modules. Another variant of the aerospike nozzle is the linear aerospike nozzle, which was envisioned for the propulsion system of the reusable launch vehicle (RLV) X-33 concept [10].

The performance characteristics and flowfield evolution of linear aerospike nozzles exhibit similarities to those of circular aerospike nozzles, with the exception of the end sides of the linear aerospike nozzle. In these regions, the surrounding flow disrupts the expanding flowfield, leading to a normal expansion of the flow relative to the main flow direction, resulting in an effective loss of performance. Additionally, the performance of plug nozzles remains relatively unchanged even when the plug is truncated at a small fraction of its length [10].

Research into aerospike thrust vectoring has explored various strategies [11–13], including movable plugs, plug-mounted flaps, and fluidic methods like differential throttling. Fluidic thrust vectoring techniques such as shock vector control [14–16], bypass shock vectoring [17], counterflow [18], co-flow [19], throat skewing, dual throat [20,21], and bypass dual throat nozzle control [22–24] demonstrate potential due to their simplicity and reliability without movable parts [12,25,26].

Differential throttling [22,27], suitable for large engines with clustered aerospike engines and multiple independent combustion chambers, allows for independent control of mass flow rate and pressure in each chamber, generating lateral thrust for maneuvering. For smaller engines where multiple combustion chambers are less practical, other fluidic thrust vectoring methods like Shock Vector Control (SVC) become viable. SVC involves injecting a secondary flow from the plug wall, creating an obstacle for the primary flow and generating lateral thrust through asymmetric pressure distribution on the nozzle walls. Effective thrust vectoring methods also minimize the reliance on large aerodynamic control surfaces during atmospheric flight.

The ongoing interest of the space community in advanced nozzles has prompted research efforts to characterize the static and dynamic behavior of these nozzles, along with innovative thrust vector control strategies. As part of this endeavor, a nozzle test rig was designed and manufactured at Politecnico di Torino (PoliTo) with the aim of laying the groundwork for future studies on advanced nozzles and their control strategies [28]. To date, numerous experiments have been conducted on linear aerospike nozzles in a Non-Differential Throttling Configuration (NDTC) at various NPRs, as detailed in [28].

In this paper, the characterization of the nozzle flow over a linear aerospike is performed by means of numerical simulations and experimental testing. The nozzle geometry used in the numerical simulation was extracted from the CAD model utilized to construct the nozzle for the experiments. The CFD analysis covers the whole operative range of the

nozzle, investigating the flowfield structure at the different NPRs. Moreover, the flow is investigated experimentally by testing the nozzle system for several NPRs in the test rig designed at PoliTo. The experimental data are used also for validating the numerical results.

The outlines of the paper are as follows: the nozzle model and the test rig setup are described in the next section; then, the mathematical model and the numerical method adopted in the CFD simulations are illustrated. The CFD and experimental data at different NPRs are collected and compared for validation. Finally, the edge effects at different NPRs have been analyzed through CFD simulations.

2. Nozzle Geometry and Experimental Setup

As a part of the JLab facility, the test-rig SPK1 was designed at PoliTo with the aim of developing a general platform for testing advanced nozzles in cold flow conditions [27,28]. The test rig provides the prescribed inlet flow conditions for the nozzle model. The system can manage interchangeable nozzle models that may be either axisymmetric (e.g., bell/dual-bell nozzle) or two-dimensional (e.g., linear aerospikes). In the latter case, an interfacing duct may be required in order to generate the planar inlet flow conditions and stream redistribution. The test rig and nozzle assembly are shown in Figure 1a.

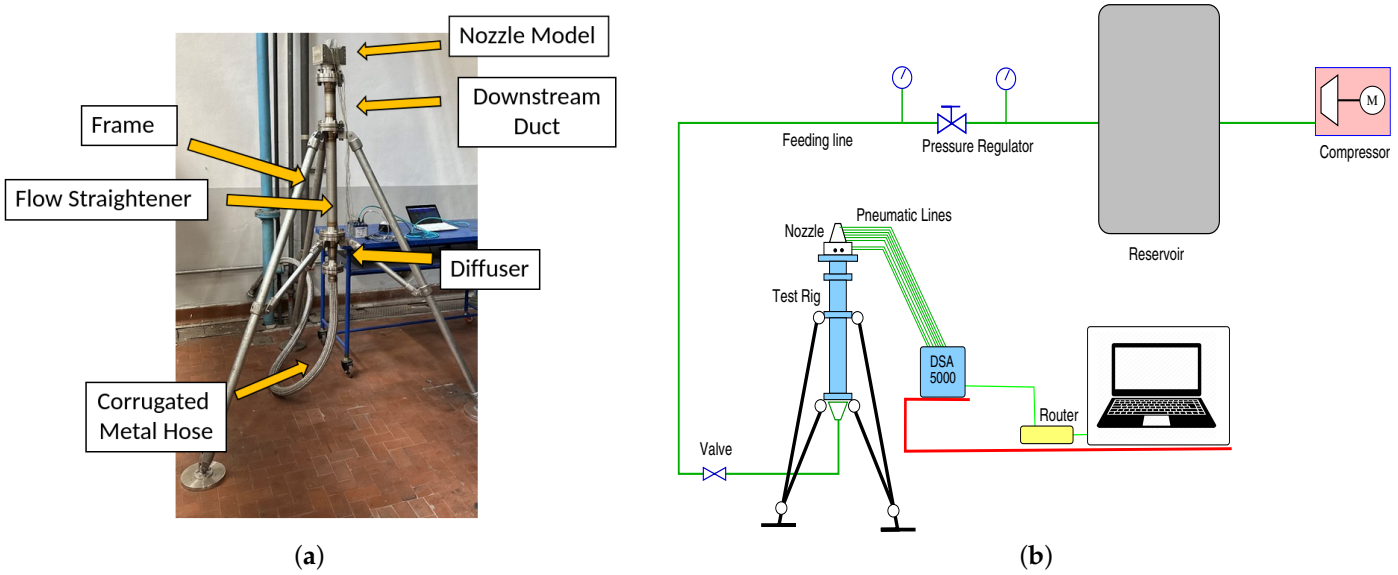

Figure 1. The JLab-SPK1 experimental apparatus: (**a**) test rig and nozzle model; (**b**) sketch of the experimental setup.

The pressure line that feeds the nozzle consists on a 25 mm pipe line at 10 bar with a 5 m^3 reservoir and a dedicated compressor. The test rig is positioned on a frame, as shown in Figure 1a. A corrugated metal hose with an inner diameter of 25 mm provides the feeding gas (air, with a regulated total pressure $p^\circ = 10$ bar and a total temperature T° of about 288 K) and is connected to a diffuser, followed by a flow straightener. The system allows for reasonable long tests with mass flow rates of the order of 1 kg/s. Further details regarding the experimental test rig can be found in Ref. [28].

A sketch of the experimental setup is presented in Figure 1b. The Scanivalve® DSA 5000 pressure scanner (Scanivalve, Liberty Lake, WA, USA) is used for measuring the mean pressure distribution along the plug profile. This pressure scanner includes sixteen temperature-compensated piezo-resistive pressure transducers allowing for fully synchronous data collection and a data stream up to 5000 Hz (samples/channel/second). One Resistance Temperature Detector (RTD) per pressure sensor is integrated in the unit and each RTD utilizes its own 24-bit A/D converter. The typical accuracy of the Scanivalve® DSA 5000 pressure scanner is ±0.04% Full Scale. The particular Scanivalve® DSA 5000 pressure scanner used in the experiments is characterized by a pressure range up to 250 psi

(1724 kPa) and a total thermal error (over 0–72 °C range) of less than ±0.001% full scale per °C. Consequently, the total uncertainty in measuring the mean pressure is evaluated to be less than 1 kPa.

A sketch of the plug profile and a picture of the nozzle model are shown in Figure 2. The nozzle profile has been designed by the classical approach, based on the method of characteristics, proposed by Angelino [29], for $\mathrm{NPR}_d = 200$. The linear plug nozzle has a width-to-height throat ratio (b/h_t) equal to 30.41. The tilt angle ϑ at the throat is equal to 68.1°. The aerospike plug is truncated at 40% of its ideal length, L_{max}. The main design parameters of the nozzle are summarized in Table 1. The static wall pressures p_w are measured via pressure ports (with a diameter is equal to 0.6 mm) drilled perpendicularly to the nozzle plug wall (see Figure 2). The distance between two adjacent pressure ports is equal to 7 mm. These ports are connected through small steel tubes and Teflon tubes to the Scanivalve® pressure scanner.

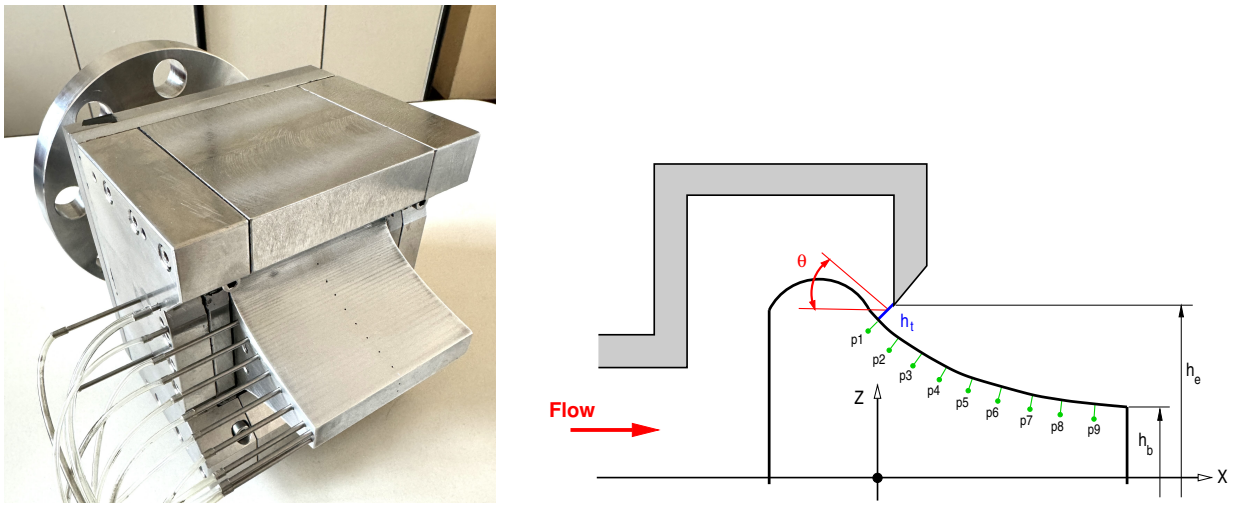

(**a**) (**b**)

Figure 2. (**a**) Aerospike nozzle model; (**b**) sketch of the plug with design parameters, and pressure tap locations (p1 to p9).

Table 1. Characteristic dimensions of the nozzle.

Quantity		Value
Throat height	h_t	2.55 mm
Throat width	b	77.55 mm
Width/height throat ratio	b/h_t	30.41
Exit section height	h_e	64.52 mm
Plug base height	h_b	12.22 mm
Throat section area	A_t	395.51 mm^2
Exit section area	A_e	5003.21 mm^2
Area ratio	A_e/A_t	12.65
Ideal aerospike length	L_{max}	133.4 mm

3. Mathematical Model and Numerical Method

The numerical framework that was adopted in this study will be briefly illustrated in this section. It is important that the numerical model and its mathematical basis are appropriate to simulate and correctly reproduce all the relevant phenomena and flow features of interest. For this work, the STAR-CCM+ software (version 18.04.009) suite was chosen to carry out all of the simulations. The choice was motivated by the great flexibility in the selection of physical and numerical models that offer a vast array of solutions to the simulation problems relevant to this topic. Moreover, extensive testing and validation of the STAR-CCM+ compressible solvers were conducted by our group, as well as by other academic and industry users.

A validation of the presented numerical framework has been performed in past research for a linear Aerospike using experimental data from the FESTIP project, as can be found in [30] .

For the solution of fluid dynamics problems, and especially for problems involving compressible fluid flows, the chosen mathematical model is represented by the unsteady Navier–Stokes equations. These equations are implemented in STAR-CCM+ using finite volume solvers through Reynolds averaging, resulting in the well-known URANS equations, written in integral form. The perfect gas equation was chosen as the model for the equation of state of the working fluid, which is dry air. Its thermophysical characteristics are determined as a function of temperature by means of Sutherland's Law for the dynamic viscosity μ and the thermal conductivity κ. The closure of the system of equations is achieved with the Spalart–Allmaras (S-A) one-equation turbulence model [31]. The S-A model is one of the four turbulence models recommended for nozzle flow simulations in reference [32] among fourteen different models investigated. The computational grid was refined near the wall to achieve a value of $Y^+ \leq 1$, and as a result, there was no need for the use of wall functions to simulate the boundary layer. The solver's numerical scheme is based on the upwind differencing concept, which takes into account the local flow characteristic to correctly propagate physical information within the domain. Inviscid fluxes are evaluated according to the AUSM+ flux–vector splitting scheme by Liou [33]. Consequently, the numerical method is capable of accurately capturing all possible fluid dynamic discontinuities present in the flowfield (i.e., shocks and contact surfaces). The spatial discretization of the numerical scheme is second-order accurate, while for the integration in time, the adopted temporal scheme is the first-order accurate Euler implicit scheme.

The computational domain consists in a polyhedral mesh, counting about 2 M cells. The conditions imposed at the boundaries of the computational domain follow the guidelines of Poinsot and Lele [34] for supersonic and subsonic mixed flows, and are presented in Figure 3. On the walls of the nozzle model, a no-slip adiabatic wall condition was imposed. The outflow boundary, on the right edge of the computational domain, features a pressure outlet condition, where a value of static pressure is imposed only for cells in which the flow is subsonic, whereas for a supersonic outflow, the pressure at the outlet is the same as the cell. The inlet conditions are imposed as total pressure and total temperature conditions, with values corresponding to the inside of the nozzle's chamber. Lastly, the other boundaries of the domain have been set to freestream conditions, where the value of static pressure, static temperature and an inlet Mach number were imposed. The Mach number was set to a very low value of 0.05 for the numerical stability of the boundaries. All simulations were carried out with a inlet total temperature $T^0 = 300$ K, an ambient pressure $p_a = 10^5$ Pa, and a turbulence viscosity ratio equal to 10, respectively.

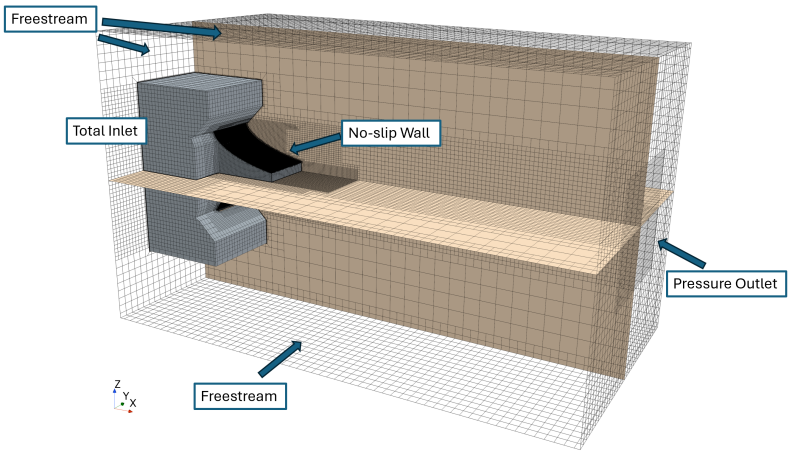

Figure 3. The computational domain with the imposed boundary conditions. The grid shows a reduced number of nodes for readability.

A grid convergence study was performed in order to select a computational grid whose size was adequate for capturing all relevant flowfield features, while at the same time being as computationally efficient as possible. Three different levels of grid refinement have been tested. These grids are characterized by 500 k, 2 M and 9 M cells, respectively. The carried out results are shown in Figure 4. From the analysis of the results shown in the figure, it can be deduced that even with the use of a medium-sized grid (2 M cells), good accuracy is achieved. Therefore, the numerical analysis was carried out using this intermediate grid.

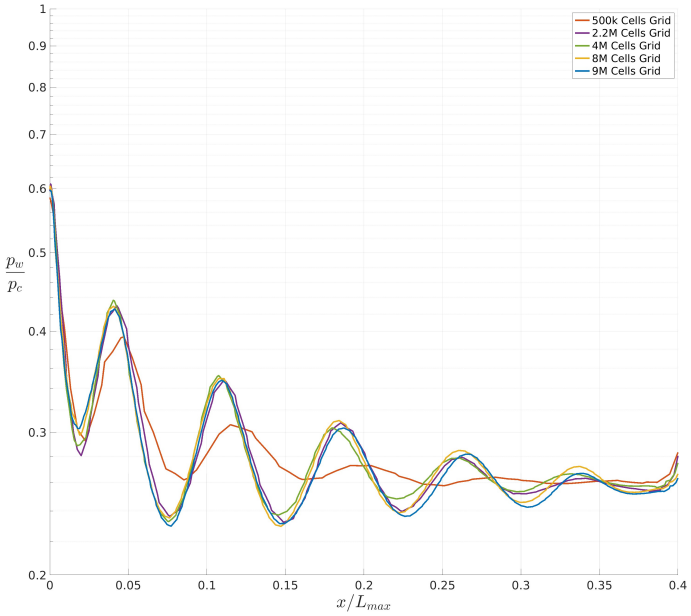

Figure 4. Distribution of wall pressure over chamber pressure p_w/p_c along the nozzle wall for the three grid levels.

4. Numerical and Experimental Results

Present investigations are based on a combination of numerical simulations and experimental testings. The nozzle performances are studied from low NPRs up to the design pressure ratio. The convergence study for determining the optimal three-dimensional grid for the numerical analysis is presented first. Then, two sets of experimental data are used for assessing and validating the accuracy of the numerical results. At higher NPR values, the study was conducted solely numerically due to the limitations of the experimental setup.

4.1. CFD and Experimental Data Comparison

An experimental test campaign was conducted to validate the numerical data obtained from the CFD calculations. Due to limitations in the experimental setup, this validation was performed at relatively low NPR values equal to 2.8 and 3.7. The pressures are measured via nine pressure taps with a diameter equal to 0.6 mm, positioned 7 mm apart, and distributed on the symmetry plane (x, z) along the wall of the plug. For each pressure tap, 450 samples are acquired with a sampling rate of 30Hz. The mean pressure distribution along the plug is then computed.

In Figures 5a and 6a, the computed Mach number fields are shown for the aerospike nozzle in working conditions at NPR $= 2.8$ and NPR $= 3.7$, respectively. Figures 5b and 6b show the numerical and experimental pressure distributions on the plug wall, normalized with chamber pressure p_w/p_c, for the same NPRs. For the nozzle in these severely over-expanded conditions, the presence of expansion and compression waves is very clearly recognizable from both the flowfield and the corresponding pressure distribution. The figures clearly demonstrate that an increase in NPR results in a natural increase in the maximum Mach number from 1.3 to 1.6. Furthermore, the wavelength of the expansion and

compression waves tends to increase as the shear layer surface moves farther apart. The maxima and minima visible in the pressure distributions of p_w/p_c gradually reduce their amplitude, with the overall expansion of the flow converging towards a value of about $p_w/p_c = 0.4$ and $p_w/p_c = 0.3$ for NPRs equal to 2.8 and 3.7, respectively. A good agreement between the numerical and experimental data in terms of pressure distribution was found. In both figures, the recirculating regions at the base of the plug are clearly visible.

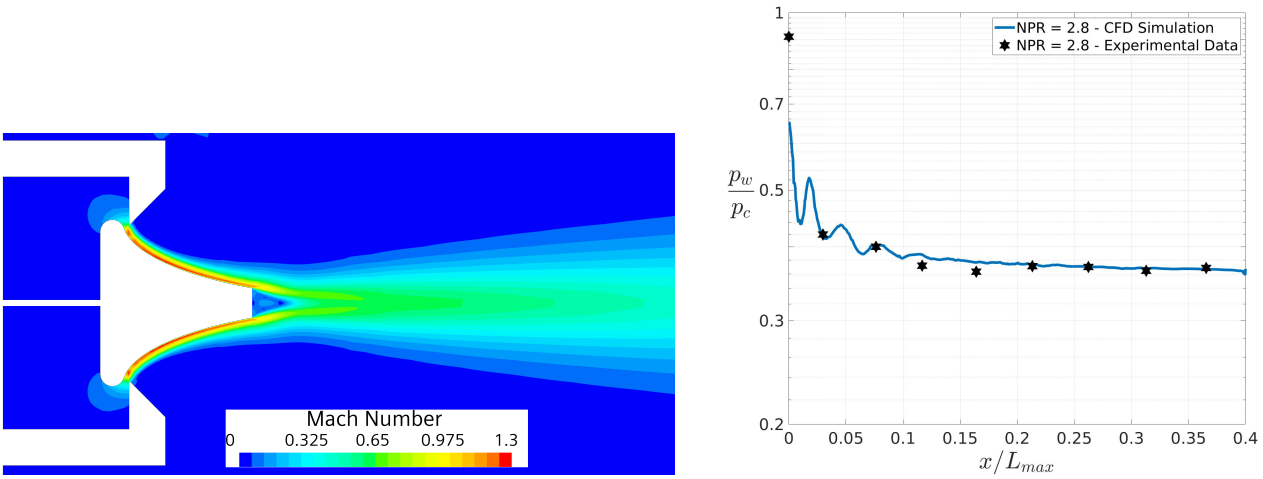

(**a**) (**b**)

Figure 5. Nozzle flowfield at NPR = 2.8. (**a**) Mach number contour map on the symmetry plane; (**b**) plot of the corresponding normalized wall pressure distribution p_w/p_c on the plug.

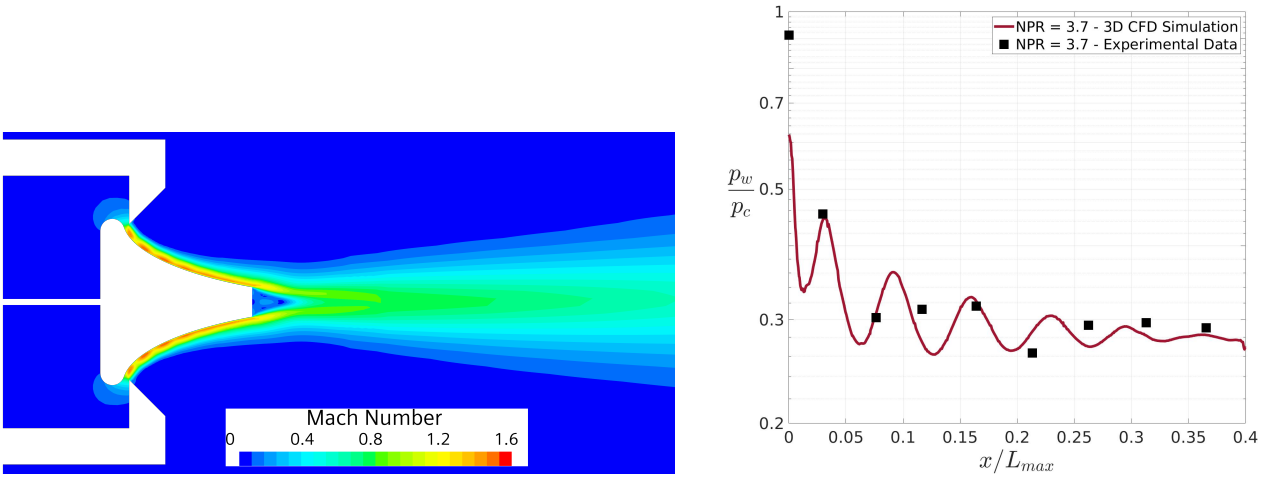

(**a**) (**b**)

Figure 6. Nozzle flowfield at NPR = 3.7. (**a**) Mach number contour map on the symmetry plane; (**b**) plot of the corresponding normalized wall pressure distribution p_w/p_c on the plug.

In Figure 7, the results for a value of NPR = 10 are shown. The expansion and compression waves are still reflected on the aerospike walls and interact with the shear layer, forming the already mentioned jet structure. The thickness of the jet region near the wall and the wavelength of the pressure distribution have both increased. As a result, the pressure peaks are now fewer and farther apart. The average expansion primarily occurs within the first 5% of the ideal plug's length, as shown in Figure 7b. Additionally, it can be seen that a recirculation zone is also present and well formed in these conditions.

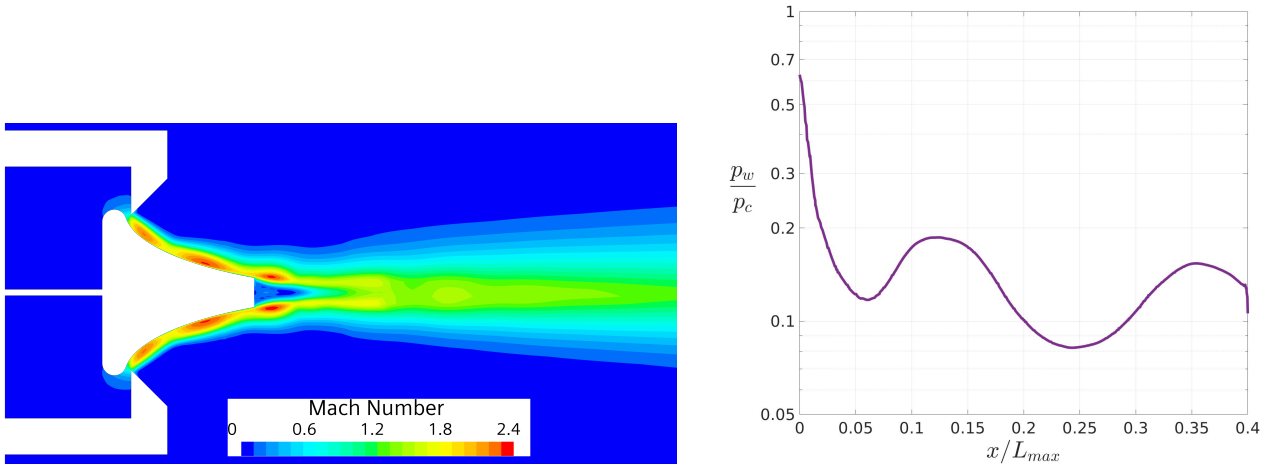

(**a**) (**b**)

Figure 7. Nozzle flowfield at NPR $= 10$. (**a**) Mach number contour map on the symmetry plane; (**b**) plot of the corresponding normalized wall pressure distribution p_w/p_c on the plug.

In Figure 8, the results for the case of NPR $= 50$ are presented. The main difference in the flowfield (Figure 8a) compared to previously observed cases is that no re-compression zones are present on the wall. Instead, there is a continuous expansion of the fluid starting from the throat and extending all the way to the end of the aerospike's wall. The wall pressure distribution shown in Figure 8b features a very steep decrease in pressure that reaches a stable value between 10 and 20% of the nozzle's ideal length L_{max}. The thickness of the jet has further increased, as well as the maximum exit Mach number realized by the nozzle. In these working conditions, the nozzle is still working in overexpanded conditions, being that it was designed for a nozzle pressure ratio of $\text{NPR}_d = 200$. However, the flowfield configuration has lost the characteristic structure of severely overexpanded conditions. The flow topology suggests that the overexpanded flow undergoes re-compression downstream of the base of the plug. Close to the recirculation zone, at the base plug, it is possible to observe the lip shocks generated in correspondence of the plug edges. Moving downstream, additional expansion occurs in the flow to recover ambient conditions, with a further increase in the Mach number up to approximately 3.6.

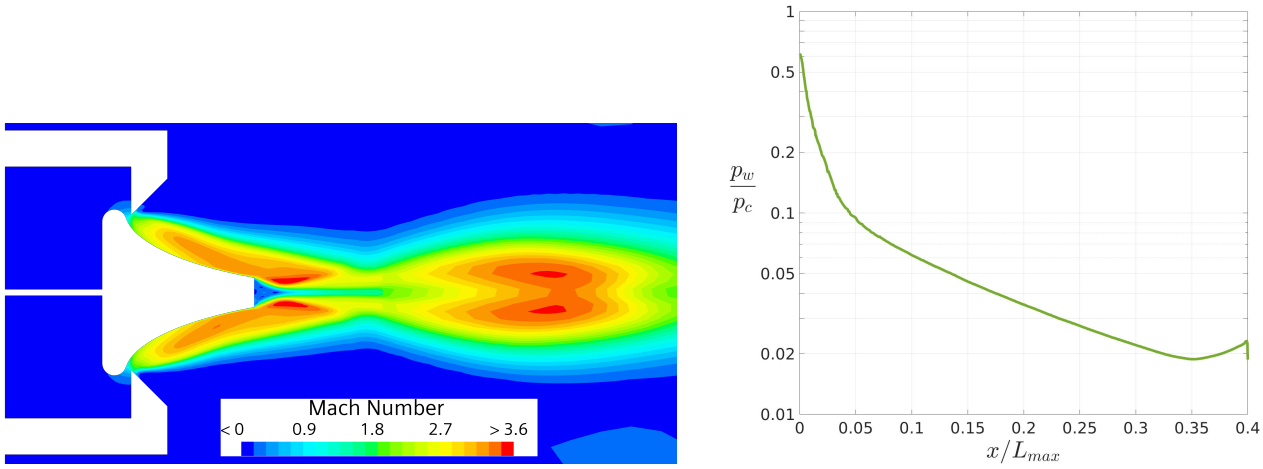

(**a**) (**b**)

Figure 8. Nozzle flowfield at NPR $= 50$. (**a**) Mach number contour map on the symmetry plane; (**b**) plot of the corresponding normalized wall pressure distribution p_w/p_c on the plug.

The results for $\text{NPR}_d = 200$ in terms of Mach iso-contours and wall pressure distribution are shown in Figure 9a and Figure 9b, respectively. From Figure 9a, it is observed that,

in the case of the design NPR_d, the shear layer no longer tends to move towards the center line, and the expansion occurs monotonically until reaching ambient pressure conditions. This design case demonstrates an almost one-dimensional exhaust flow (see e.g., [2]).

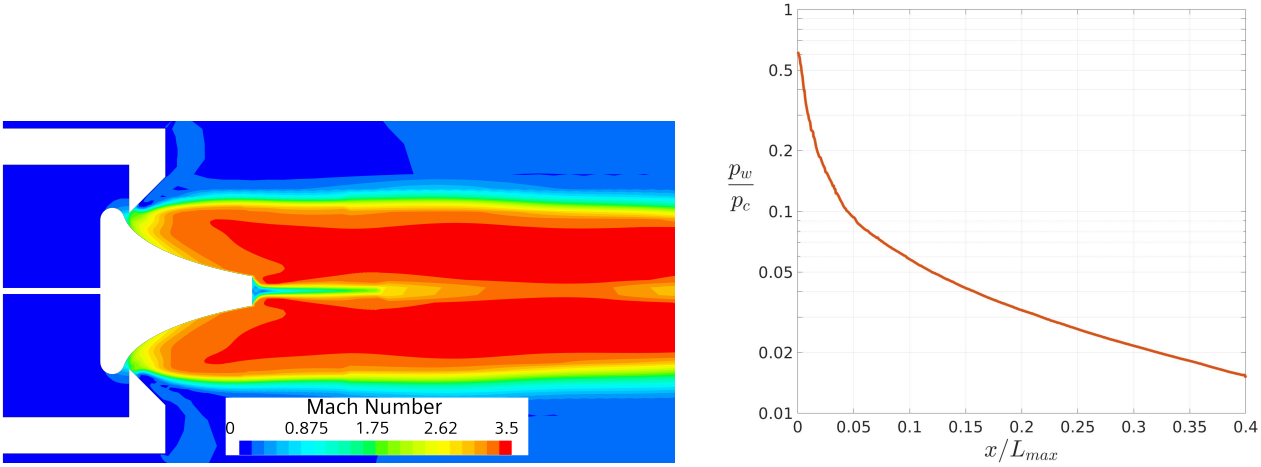

Figure 9. Nozzle flowfield at NPR $= 200$. (**a**) Mach number contour map on the symmetry plane; (**b**) plot of the corresponding normalized wall pressure distribution p_w/p_c on the plug.

All the previously presented pressure distributions along the plug wall are summarized in Figure 10. The complex scenario obtained at low NPR, well captured by numerical and experimental results, can be clearly seen. The number of expansion and re-compression waves, generated by the interaction with the slip surface, tends then to decrease as the NPR becomes higher and higher, until a monotonic expansion is reached for $\text{NPR}_d = 200$.

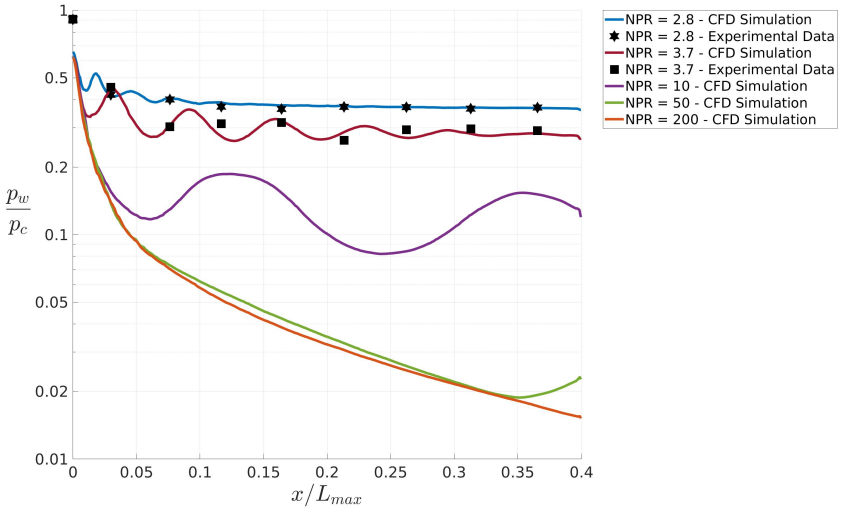

Figure 10. Distribution of wall pressure over chamber pressure p_w/p_c along the nozzle wall for all values of NPR considered.

4.2. Analysis of the Flowfield Side Effects

The aim of this section is to highlight the three-dimensional flowfield behaviour due to the finite span of the plug. This is accomplished through the visualization of the flow and the analysis of pressure distributions on the wall along the spanwise direction of the plug for different NPR values. In Figure 11a, a three-dimensional view of the nozzle is presented. The colormap of the absolute static pressure on the plug surface, along with the Mach number flowfield on the (x, z) symmetry plane, are shown for NPR $= 3.7$. The

three-dimensional nature of the pressure distribution on the wall surface of the plug is observable; the band structure with compression zones (in red) and expansion zones (in green) is clearly evident. This band structure is associated with variations in the Mach number observable in the (x, z) symmetry plane.

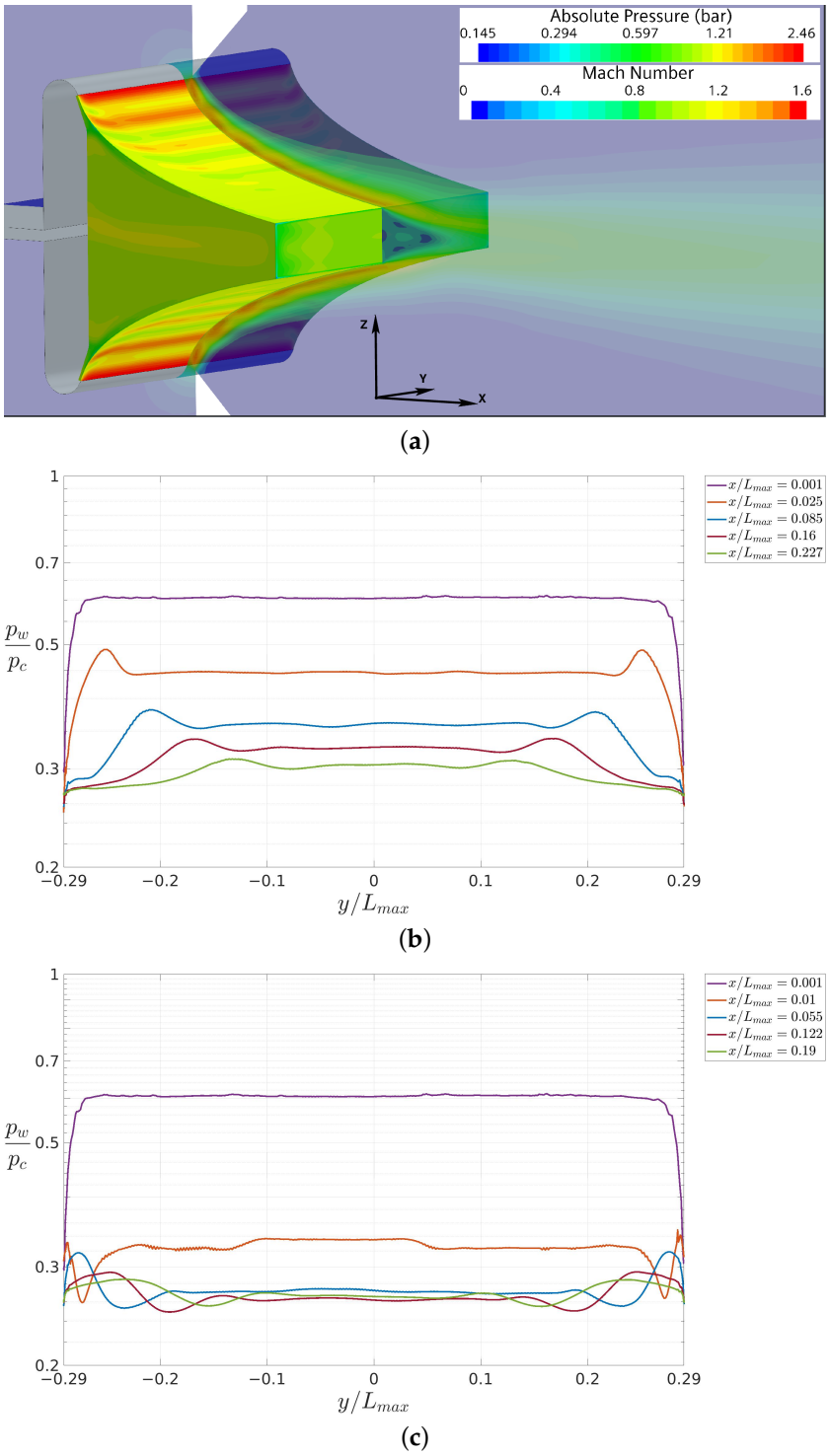

Figure 11. Three-dimensional flowfield at NPR $= 3.7$. (**a**) Colormap of absolute static pressure and Mach number flowfield in the (x, z) symmetry plane; (**b**) spanwise wall pressure distributions p_w/p_c at different streamwise locations taken in correspondence of the pressure maxima shown in Figure 6b; (**c**) spanwise wall pressure distributions p_w/p_c at different streamwise locations taken in correspondence of the pressure minima shown in Figure 6b.

In Figure 11b,c, the spanwise pressure distributions on the plug wall at different streamwise locations are shown for the case at NPR = 3.7. The streamwise locations have been chosen corresponding to the maximum and minimum values of the pressure distribution along the x-axis direction observed in the symmetry plane (see Figure 6b), respectively. It can be observed that at different streamwise positions, there is a sufficiently wide region where the pressure remains almost constant. However, three-dimensional effects are clearly visible going towards the sides of the plug, and become more relevant at the end of the nozzle. In Figure 11b, the re-compression regions originated from the nozzle throat evolving towards the center line of the linear plug are shown. In Figure 11c, the presence of minima in the pressure distribution suggests the occurrence of expansion waves on the sides of the previously described re-compression regions.

The side effects are more remarkable when evaluating configurations at low values of NPR, that is when the nozzle is working in overexpanded conditions, and the system of expansion and re-compression waves is generated to automatically adapt the nozzle to the external ambient conditions. In Figure 12, the spanwise pressure distributions along the wall are presented for the nozzle working at $\mathrm{NPR}_d = 200$. The change in flow structure is evident with the absence of re-compression regions at the sides of the plug. Only monotonic expansions in the spanwise direction are observable.

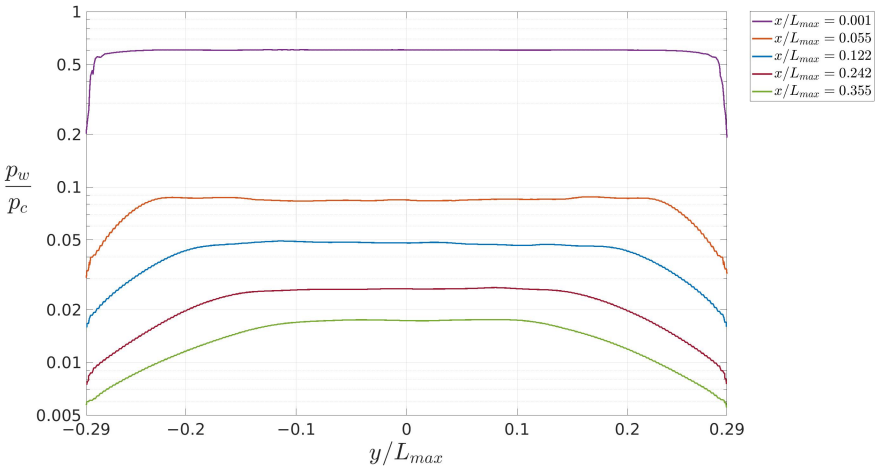

Figure 12. Spanwise wall pressure distributions p_w/p_c at different streamwise locations for NPR = 200.

In Figure 13, the vorticity contour fields at different axial sections are shown. Notably, the highest values of the vorticity are concentrated in the boundary layer and in the recirculation bubble that forms at the truncation of the plug. As we move away from the plug, the vorticity gradually diffuses into the flowfield. Moreover, the evolution of the previously described structures forming at the sides of the plug is clearly observable at different axial positions.

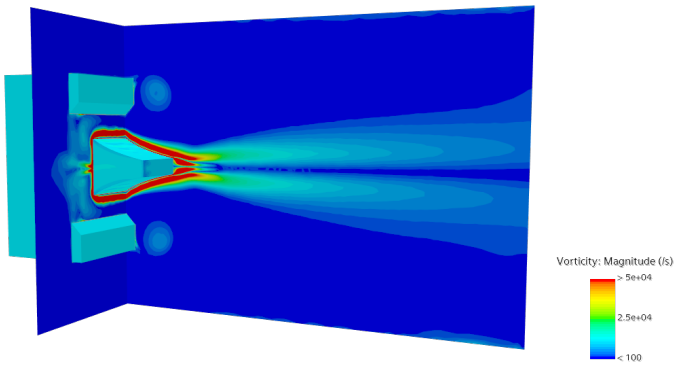

(**a**)

Figure 13. *Cont.*

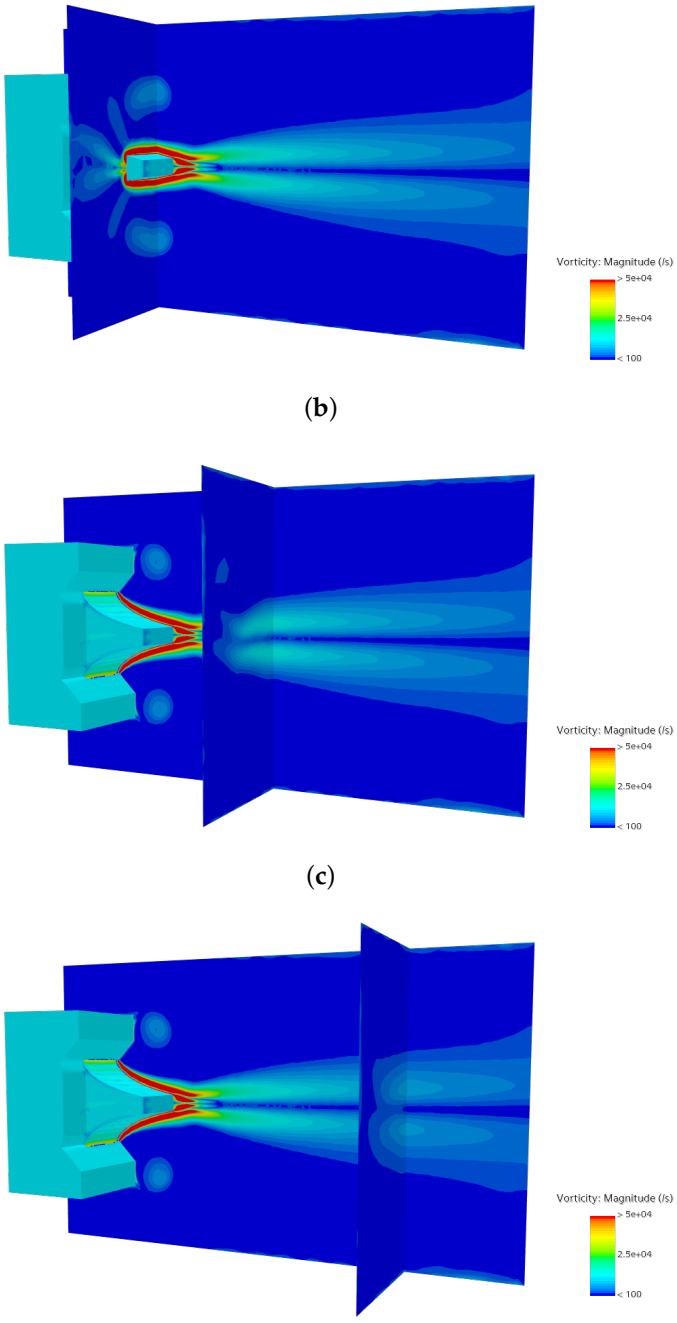

Figure 13. Colormap of vorticity magnitude at NPR = 3.7 for different axial positions: (**a**) $x/L_{max} = 0.07$, (**b**) $x/L_{max} = 0.3$, (**c**) $x/L_{max} = 1.05$ and (**d**) $x/L_{max} = 1.80$.

5. Conclusions

The flow over a 40% truncated linear aerospike was studied by combining theoretical grounds, numerical simulations and experimental tests. The numerical investigations are based on three-dimensional CFD simulations at different operating conditions on the actual geometry of the nozzle model tested experimentally. The experimental results have validated the numerical results obtained at the corresponding NPRs. At higher pressure ratios, the flowfield characterization is completed by CFD analyses only. The three-dimensional flow features due to the finite span of the plug are investigated. A system of expansion and re-compression waves is generated at the sides of the plug when the nozzle is working in overexpanded conditions. It is also noticed that these three-dimensional effects become

more relevant at the end of the nozzle. The absence of re-compression regions at the sides of the plug is observable when the nozzle is working at the design conditions.

Author Contributions: Conceptualization, R.M., G.M.D.C. and M.F.; methodology, R.M., G.M.D.C. and M.F.; software, R.M., E.R. and M.F.; validation, R.M., G.M.D.C., E.R. and M.F.; formal analysis, R.M., G.M.D.C. and M.F.; investigation, R.M., G.M.D.C., E.R. and M.F.; resources, R.M., G.M.D.C. and M.F.; data curation, R.M., G.M.D.C., E.R. and M.F.; writing—original draft preparation, R.M., G.M.D.C., E.R. and M.F.; writing—review and editing, R.M., G.M.D.C., E.R. and M.F.; visualization, R.M., G.M.D.C., E.R. and M.F.; supervision, R.M., G.M.D.C. and M.F. All authors have read and agreed to the published version of the manuscript.

Funding: This research received no external funding.

Data Availability Statement: The datasets presented in this article are not readily available because they are part of an ongoing study, further inquiries can be directed to the corresponding author.

Acknowledgments: Computational resources were provided by hpc@polito.it, a project of Academic Computing within the Department of Control and Computer Engineering at the Politecnico di Torino (http://www.hpc.polito.it).

Conflicts of Interest: The authors declare no conflicts of interest.

Nomenclature

A_e	= Exit section area $[\text{mm}^2]$
A_t	= Throat section area $[\text{mm}^2]$
b	= Plug width [mm]
h_b	= Plug base height [mm]
h_e	= Exit section height [mm]
h_t	= Throat height [mm]
L_{max}	= Ideal aerospike length [mm]
p_a	= Ambient pressure [bar]
p_c	= Static chamber pressure [bar]
p_c°	= Total chamber pressure [bar]
p_w	= Static wall pressure [bar]
θ	= Throat tilt angle [deg]
μ	= Dynamic viscosity $[\text{Pa} \cdot \text{s}]$
κ	= Thermal conductivity $[\text{W}/(\text{m} \cdot \text{K})]$
NPR	= Nozzle pressure ratio, p_c° / p_a
NPR_d	= Design nozzle pressure ratio, $(p_c^\circ / p_a)_d$

References

1. Guo, C.; Wei, Z.; Xie, K.; Wang, N. Thrust Control by Fluidic Injection in Solid Rocket Motors. *J. Propuls. Power* **2017**, *33*, 815–829. [CrossRef]
2. Hagemann, G.; Immich, H.; Van Nguyen, T.; Dumnov, G. Advanced rocket nozzles. *J. Propuls. Power* **1998**, *14*, 620–634. [CrossRef]
3. Manski, D. *Clustered Plug Nozzles for Future European Reusable Rocket Launchers*; German Aerospace Research Establishment, Lampoldshausen: Baden-Württemberg, Germany, 1981; pp. 643–681.
4. Dumnov, G.; Nikulin, G.; Ponomaryov, N. Investigation of advanced nozzles for rocket engines. *Space Rocket Eng. Power Plants* **1993**, *4*, 10–12.
5. Reijasse, P.; Gorbel, B. Experimental analysis of the supersonic flow confluence past a jet-on axisymmetric afterbody. In Proceedings of the 14th Applied Aerodynamics Conference, New Orleans, LA, USA, 17–20 June 1996; p. 2449.
6. Tomita, T.; Tamura, H.; Takahashi, M. An experimental evaluation of plug nozzle flowfield. In Proceedings of the 32nd Joint Propulsion Conference and Exhibit, Lake Buena Vista, FL, USA, 1–3 July 1996; p. 2632.
7. Takahashi, H.; Tomioka, S.; Sakuranaka, N.; Tomita, T.; Kuwamori, K.; Masuya, G. Experimental Study on the Aerodynamic Performance of Clustered Linear Aerospike Nozzles. In Proceedings of the 18th AIAA/3AF International Space Planes and Hypersonic Systems and Technologies Conference, Tours, France, 24–28 September 2012; p. 5933.
8. Hao, Z.; Tian, H.; Guo, Z.; Hedong, L.; Li, C. Numerical and experimental investigation of throttleable hybrid rocket motor with aerospike nozzle. *Aerosp. Sci. Technol.* **2020**, *106*, 105983.

9. Besnard, E.; Chen, H.H.; Mueller, T.; Garvey, J. Design, manufacturing and test of a plug nozzle rocket engine. In Proceedings of the 38th AIAA/ASME/SAE/ASEE Joint Propulsion Conference & Exhibit, Indianapolis, Indiana, 7–10 July 2002; p. 4038.
10. The Linear Aerospike Engine. 1998. From X-33 Prog OFC 8055725801, NASA. Available online: https://ntrs.nasa.gov/api/citations/19990004339/downloads/19990004339.pdf (accessed on 28 June 2024).
11. Bach, C.; Schongarth, S.; Bust, B.; Propst, M.; Sieder-Katzmann, J.; Tajmar, M. How to steer an aerospike. In Proceedings of the 69th International Astronautical Congress (IAC), Bremen, Germany, 1–5 October 2018.
12. Saadia, A.; Tariq, A.K. Techniques of Fluidic Thrust Vectoring in Jet Engine Nozzles: A Review. *Energies* **2023**, *16*, 5721. [CrossRef]
13. Warsop, C.; Crowther, W. Fluidic Flow Control Effectors for Flight Control. *AIAA J.* **2018**, *56*, 3808–3824. [CrossRef]
14. Deng, R.; Setoguchi, T.; Dong Kim, H. Large eddy simulation of shock vector control using bypass flow passage. *Int. J. Heat Fluid Flow* **2016**, *62*, 474–481. [CrossRef]
15. Waithe, K.; Deere, K. An Experimental and Computational Investigation of Multiple Injection Ports in a Convergent-Divergent Nozzle for Fluidic Thrust Vectoring. In Proceedings of the 21st AIAA Applied Aerodynamics Conference, Orlando, FL, USA, 23–26 June 2003; AIAA Paper 2003-3802.
16. Forghany, F.; Taeibe-Rahni, M.; Asadollahi-Ghohieh, A.; Banazdeh, A. Numerical investigation of injection angle effects on shock vector control performance. *Proc. Inst. Mech. Eng. Part G J. Aerosp. Eng.* **2017**, *233*, 405–417. [CrossRef]
17. Wang, Y.; Xu, J.; Huang, S.; Lin, Y.; Jiang, J. Computationl study of axisymmetric divergent bypass dual throat nozzle. *Aerosp. Sci. Technol.* **2019**, *86*, 177–190. [CrossRef]
18. Kexin Wu, K.; Kim, H.; Jin, Y. Fluidic thrust vector control based on counter-flow concept. *Proc. Inst. Mech. Eng. Part G J. Aerosp. Eng.* **2019**, *233*, 1412–1422.
19. Banazadeh, A.; Saghafi, F. An investigation of empirical formulation and design optimisation of co-flow fluidic thrust vectoring nozzles. *Aeronaut. J.* **2016**, *121*, 213–236. [CrossRef]
20. Deere, K.; Flamm, J.; Berrier, B.; Johnson, S. Computational Study of an Axisymmetric Dual Throat Fluidic Thrust Vectoring Nozzle for a Supersonic Aircraft Application. In Proceedings of the 43rd AIAA/ASME/SAE/ASEE Joint Propulsion Conference & Exhibit, Cincinnati, OH, USA, 8–11 July 2007; AIAA Paper 2007-5085.
21. Flamm, J.; Deere, K.; Mason, M.; Berrier, B.; Johnson, S. Experimental Study of an Axisymmetric Dual Throat Fluidic Thrust Vectoring Nozzle for a Supersonic Aircraft Application. In Proceedings of the 43rd AIAA/ASME/SAE/ASEE Joint Propulsion Conference & Exhibit, Cincinnati, OH, USA, 8–11 July 2007; AIAA Paper 2007-5084.
22. Ferlauto, M.; Ferrero, A.; Marsicovetere, M.; Marsilio, R. Differential Throttling and Fluidic Thrust Vectoring in a Linear Aerospike. *Int. J. Turbomach. Propuls. Power* **2021**, *6*, 8. [CrossRef]
23. Resta, E.; Marsilio, R.; Ferlauto, M. Thrust vectoring of a fixed axisymmetric supersonic nozzle using the Shock-Vector Control method. *Fluids* **2021**, *6*, 441. [CrossRef]
24. Wang, Y.; Xu, J.; Huang, S.; Jiang, J.; Pan, R. Design and Preliminary Analysis of the Variable Axisymmetric Divergent Bypass Dual Throat Nozzle. *J. Fluids Eng.* **2020**, *142*, 061204. [CrossRef]
25. Páscoa, J.; Dumas, A.; Trancossi, M.; Stewart, P.; Vucinic, D. A review of thrust-vectoring in support of a V/STOL non-moving mechanical propulsion system. *Open Eng.* **2013**, *3*, 374–388. [CrossRef]
26. Zmijanovic, V.; Leger, L.; Sellam, M.; Chpoun, A. Assessment of transition regimes in a dual-bell nozzle and possibility of active fluidic control. *Aerosp. Sci. Technol.* **2018**, *82*, 1–8. [CrossRef]
27. Di Cicca, G.M.; Hassan, J.; Resta, E.; Marsilio, R.; Ferlauto, M. Experimental Characterization of a Linear Aerospike Nozzle Flow. In Proceedings of the 2023 IEEE 10th International Workshop on Metrology for AeroSpace (MetroAeroSpace), Milan, Italy, 19–22 June 2023.
28. Bonnet, V.; Ortone, F.; Di Cicca, G.M.; Marsilio, R.; Ferlauto, M. Cold Gas Measurement System for Linear Aerospike Nozzles. In Proceedings of the 2022 IEEE 9th International Workshop on Metrology for AeroSpace (MetroAeroSpace), Pisa, Italy, 27–29 June 2022.
29. Angelino, G. Approximate method for plug nozzle design. *AIAA J.* **1964**, *2*, 1834–1835. [CrossRef]
30. Ferlauto, M.; Ferrero, A.; Marsilio, R. Shock Vector Control Technique for Aerospike Nozzles. In Proceedings of the AIAA Scitech 2020 Forum, Orlando, FL, USA, 6–10 January 2020.
31. Spalart, P.; Allmaras, S. A One-Equation Turbulence Model for Aerodynamic Flows. *Rech. Aerosp.* **1994**, *1*, 5–21.
32. Tian, C.; Lu, Y. Turbulence Models of Separated Flow in Shock Wave Thrust Vector Nozzle. *Eng. Appl. Comput. Fluid Mech.* **2013**, *7*, 182–192. [CrossRef]
33. Liou, M.S. A sequel to ausm: Ausm+. *J. Comput. Phys.* **1996**, *129*, 364–382. [CrossRef]
34. Poinsot, T.; Lele, S. Boundary conditions for direct simulations of compressible viscous reacting flows. *J. Comput. Phys.* **1992**, *101*, 104–129. [CrossRef]